Interferograms, Schlieren, and Shadowgraphs Constructed from Real- and Ideal-Gas, Two- and Three-Dimensional Computed Flowfields

Leslie A. Yates
Eloret Institute
Palo Alto, California

Abstract

The construction of interferograms, schlieren, and shadowgraphs from computed flowfield solutions permits one-to-one comparisons of computed and experimental results. A method for constructing these images from both ideal- and real-gas, two- and three-dimensional computed flowfields is described. The computational grids can be structured or unstructured, and multiple grids are an option. Constructed images are shown for several types of computed flows including nozzle, wake, and reacting flows; comparisons to experimental images are also shown. In addition, the sensitivity of these images to errors in the flowfield solution is demonstrated, and the constructed images can be used to identify problem areas in the computations.

Introduction

The development of techniques for comparing computed flowfield solutions with experimental interferograms, schlieren, and shadowgraphs is vital for validation of ideal- and real-gas computational fluid dynamics (CFD) codes. Infinite- and finite-fringe interferograms can be transformed into density fields only for two-dimensional (2-D) and axially symmetric non-reacting flows. In experimental schlieren and shadowgraphs, several flow features including shocks, shear layers, and expansion fans are recorded. When flow solutions are compared to these images, contour plots for only one plane of data, usually the symmetry plane, are typically used. If the flow is three dimensional or the model is free to roll, no single computational plane provides all the information necessary for realistic comparisons to experimental images.

The information required for the construction of interferograms, schlieren, and shadowgraphs is contained in the flowfield solutions. By developing routines to evaluate and integrate appropriate functions of the refractive index (n), direct comparisons of computed and experimental results can be made. Constructed interferograms provide the basis for quantitative comparisons of line integrals of n for reacting flows and the integrated density for non-reacting flows. With constructed schlieren and shadowgraphs, the computed and experimental locations of shocks, shear layers, expansion fans, separation, and reattachment can be compared. Constructed schlieren can also be used to compare signs of line integrals of the gradient of n.

In this paper, CISS (Constructed Interferograms, Schlieren, and Shadowgraphs) is described. CISS is software that constructs images from ideal- and real-gas, 2-D, axially symmetric, and 3-D computed flowfield solutions. The computational grids can be structured or unstructured, and multiple grids are an option. Results are shown for several types of flowfields, and the effects of grid resolution and solution convergence are discussed. Comparisons to experimental images are also included.

Constructing Numerical Interferograms, Schlieren, and Shadowgraphs

Construction of interferograms, schlieren, and shadowgraphs from flowfield solutions requires three steps: 1) identifying and evaluating the appropriate functions of n, 2) integrating these functions along lines of sight, and 3) post-processing the integrals to give the desired images. In this section, these three processes will be described.

Functions of the Refractive Index used in Constructing Images

As light passes through the flowfield, the phase shift and angle of deflection are obtained by integrating functions of the refractive index along lines of sight. For ideal and non-reacting gases, the refractive index is simply

$$n = 1 + \kappa\rho$$

where κ is the appropriate Gladstone-Dale constant for the gas and ρ is the density. For both equilibrium and nonequilibrium real-gas computations, the species mass fractions vary throughout the flow, and the refractive index is given by the sum of the contribution from each gas,[1]

$$n = 1 + \sum_i \kappa_i \rho_i$$

Here, κ_i is the Gladstone-Dale constant and ρ_i is the partial density for the ith species.

Interferograms measure the phase shift between reference and object beams caused by variations in the refractive index throughout the flowfield. When calculating interferograms from computational flowfields, the phase shift is obtained by integrating

$$f(n) = \frac{2\pi}{\lambda}(n - n_0)$$

along a line of sight. Here, n_0 is the refractive index of the undisturbed flow and λ is the wavelength of the light.

Schlieren are created in the laboratory by passing collimated light through the flowfield, focusing this light to a finite-sized point, using a knife edge to block out a portion of the light, and then re-focusing the remaining light onto an image plane

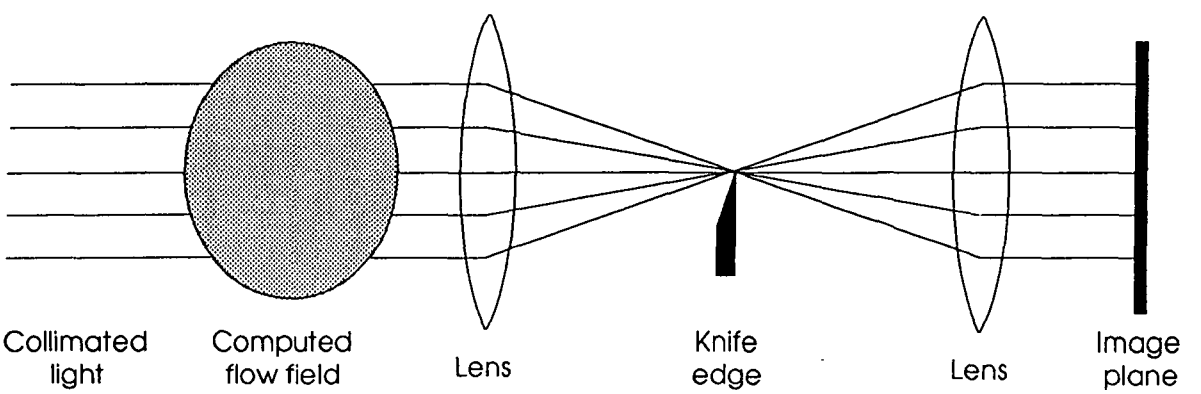

Figure 1. Schematic for constructing schlieren.

(Fig. 1). The amount of light blocked by the knife edge is proportional to the angular deflection of the light; the deflection is caused by gradients in the refractive index. The incremental change in the angular deflection at any point in the flowfield is

$$\delta\varepsilon_x = f(n) = \frac{1}{n}\frac{\partial n}{\partial x} \qquad \text{and} \qquad \delta\varepsilon_y = f(n) = \frac{1}{n}\frac{\partial n}{\partial y}$$

Integrating these functions through the flowfield solution gives the total angular deflections, ε_x and ε_y.

In shadowgraphs, the image plane is not focused in the flowfield, but at some distance from it, and the dark and light regions are caused by the concentration and divergence of light. In many text books (e.g., Refs. 2 and 3), the function used for constructing shadowgraphs is the line integral of the second derivative of the refractive index. In CISS, the function used for constructing shadowgraphs has been chosen to be equal to that used for schlieren. At the exit of the computational flowfield, the angular deflection is known. If the distance to the image plane is also known, then the location on the image plane where the deflected light falls is known. The shadowgraph is constructed by adding the contribution of the deflected light beams at each point on the image plane. Using this method, the thickness of the dark and bright regions is partially controlled by the position of the image plane. This dependency of the dark and bright regions on the image plane's position is observed in experimental shadowgraphs.

Integration Scheme

Tracing the actual light path as it bends through the computational flowfield and integrating the appropriate function of the refractive index along this path is computationally expensive. The resources required for producing constructed images can be reduced by approximating the light's path by a straight line perpendicular to the image plane. For regions of the flow without shocks, this approximation should have a minimal effect on the constructed images. In shock regions, the index of refraction changes rapidly, and the approximation may introduce errors; however, these errors are in many cases on the order of or smaller than the solution and experimental errors.

This approximation minimizes the need for search routines, and interferograms, schlieren, and shadowgraphs can be constructed without any ray tracing. For instance, consider an image defined by an $M \times N$ array of light 'cells.' The value of the integral for the m,n element of the array is given by

$$A_{m,n} = \int_0^z f\,[n(x_m, y_n, \zeta)]\, d\zeta$$

where the image plane is located at z and (x_m, y_n) are the x,y-coordinates of the light cell at the m,n location in the array. The integration path can be broken into several segments

$$A_{m,n} = \sum_{i=1}^{N} \int_{z_i}^{z_{i+1}} f\,[n(x_m, y_n, \zeta)]\, d\zeta$$

In this expression, the line of integration enters the ith computational cell at z_i and exits it at z_{i+1} (Fig. 2). In the actual solution procedure, no ray tracing of the line of inte-

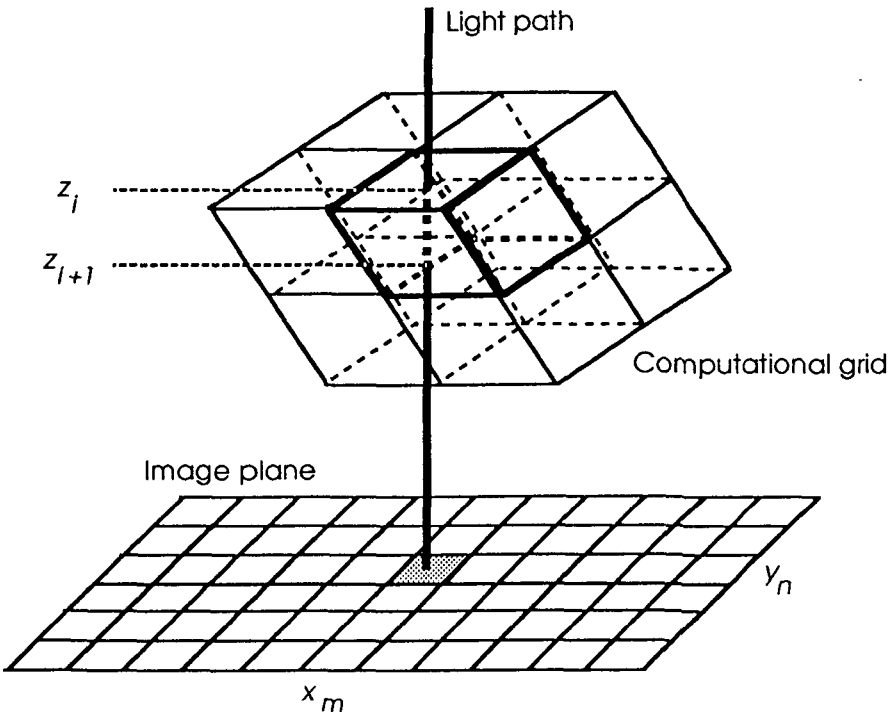

Figure 2. Schematic for integration process.

gration through the flowfield is necessary. By assuming minimal deflection of the light through the flowfield and approximating the light's path by a straight line, the contribution of each computational cell to the line integral can be found independently, and the order of evaluation and summation has no effect on the final result. Therefore, for each computational cell, the integrals

$$\int_{z_i}^{z_{i+1}} f\,[n(x_m, y_n, \zeta)]\, d\zeta$$

are evaluated for every x_m, y_n that fall within the cell, and the value of the integral is added to the appropriate location on the image plane.

The test for determining if the point x_m, y_n falls within the computational cell is as follows. First, to minimize the number of tests required, the maximum and minimum x and y values for the computational cell are found. Then the surfaces of the computational cell are described by triangles, and for each triangle, three cross products are formed:

$$(\vec{x}_1 - \vec{x}_{mn}) \times (\vec{x}_1 - \vec{x}_2)$$
$$(\vec{x}_2 - \vec{x}_{mn}) \times (\vec{x}_2 - \vec{x}_3)$$
$$(\vec{x}_3 - \vec{x}_{mn}) \times (\vec{x}_3 - \vec{x}_1)$$

In these equations, $\vec{x}_{mn}$ gives the position of the light cell, and $\vec{x}_1$, $\vec{x}_2$, and $\vec{x}_3$ are the projections onto the image plane of the vertices of the triangle. Testing is performed

only for the x_m and y_n that lie within the minimum and maximum x and y values for the computational cell. The sign for all three cross products is the same if and only if the point lies within the triangle, and the triangular surfaces through which the line of integration enters and exits the computational cell can be determined. Once these surfaces are determined, interpolated values for z_i, z_{i+1}, $f(x_m, y_n, z_i)$, and $f(x_m, y_n, z_{i+1})$ at the entrance and exit are obtained, and the line integral is evaluated. In CISS, three functions of the refractive index are integrated simultaneously: $n-1$, $(1/n)\partial n/\partial x$, and $(1/n)\partial n/\partial y$.

Construction of the Images

For infinite-fringe interferograms, the image intensity is simply proportional to the sine of the phase shift ϕ:

$$\phi = \frac{2\pi}{\lambda} \int_0^z (n - n_0)\, d\zeta$$

For finite-fringe interferograms, an additional phase is added:

$$\delta\phi = k_x x + k_y y$$

and the spacing and orientation of the freestream fringes are determined by k_x and k_y.

For schlieren, the intensity is a function of the angular deflection. As an example, consider a horizontal knife edge (Fig. 1) and a rectangular section of the initial light source with height h. As the rectangular section of the light source passes through the flowfield, it is deflected and exits the flow at an angle. When the light exiting from the flowfield is then focussed to a finite-sized dot at the plane of the knife edge, the rectangular element has a height of h', and it has been deflected vertically by $\kappa\varepsilon_y$; κ is a function of the distance between the flowfield and the knife edge. There is also a horizontal deflection; however, it is unimportant in this case. If the horizontal knife edge is placed at the center of the plane, the ratio of light not blocked by the knife edge to the amount of the original light is

$$\begin{array}{lll} 0 & \text{for} & \dfrac{\kappa\varepsilon_y}{h'} \le -\dfrac{1}{2} \\ 1 & \text{for} & \dfrac{\kappa\varepsilon_y}{h'} \ge \dfrac{1}{2} \\ \dfrac{1}{2} + \dfrac{\kappa\varepsilon_x}{h'} & \text{for} & -\dfrac{1}{2} < \dfrac{\kappa\varepsilon_y}{h'} < \dfrac{1}{2} \end{array}$$

The intensity patterns in the schlieren are proportional to the square of this ratio.

As mentioned previously, shadowgraphs are not constructed in CISS from line integrals of second derivatives of the refractive index. Instead they are given by variations in the intensity caused by the deflection of the light. The location and size of a square element of light after it passes through the flowfield is determined by the deflection of light sources that define the corners of the element. The total angular deflection for these light sources is a function of the angle at which the light exits the flowfield; that is, shadowgraphs are also governed by ε_x and ε_y. The deflected square

element is then projected onto the image plane, and the amplitude of the electric field at each *i,j*-element in the image plane is increased by

$$\Delta E_{ij} = E_o \frac{B_f \cap A_{ij}}{B_i}$$

Here, E_o is the amplitude of the initial field, $B_f \cap A_{ij}$ is the area of the intersection of the deflected element with the *i,j*-element of the image plane, and B_i is the initial area of the deflected element. The intensity pattern observed in the shadowgraph is proportional to the square of the E_{ij}'s.

The time requirements for constructing these images from simulated flowfields are linearly proportional to the grid size and the number of pixels defining the image. For 2-D flowfields, the image construction takes only a few seconds on a CRAY-YMP. For 3-D images defined by 400,000 pixels, construction using flowfield solutions with 250,000 grid points takes a few minutes.

Constructed Images

Representative images are shown in this section for several types of hypersonic flows including ramp, nozzle, reacting, and blunt-body flows. In Fig. 3, constructed and experimental schlieren are shown for a 2-D, 15° compression corner; a horizontal knife edge was used for both the schlieren. The shocks, shear layers, and separation region observed in the experimental schlieren are simulated by the constructed schlieren. The dark regions in the constructed schlieren are caused by rapid increases in density across the computed shocks, and they correspond to dark regions in the experimental schlieren. The light regions in both the constructed and experimental schlieren are identified with shear layers, and they are caused by density gradients near the surface. These shear layers lift off the surface when separation occurs, and the extent of the computed and experimental separation regions can be compared. The sharpness of the features in the constructed schlieren can be further improved by using grid adaptation to reduce solution errors.

In Fig. 4, constructed and experimental shadowgraphs for a generic, National Aerospace Space Plane (NASP) nozzle configuration, the Single Expansion Ramp Nozzle (SERN), are shown. Both the freestream and nozzle flows are supersonic. The

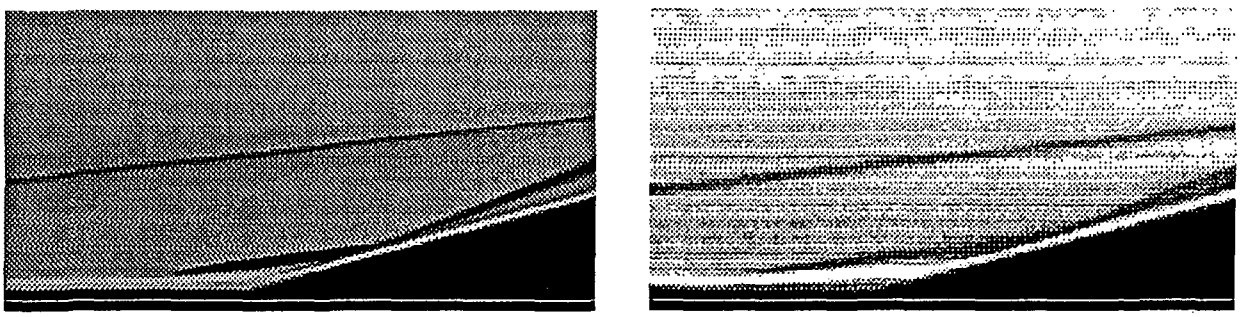

Constructed schlieren Experimental schlieren

Figure 3. Constructed and experimental schlieren for a two-dimensional compression corner. Flow solution: Tokarcik et al.;[4] experiment: Delery and Coet.[5]

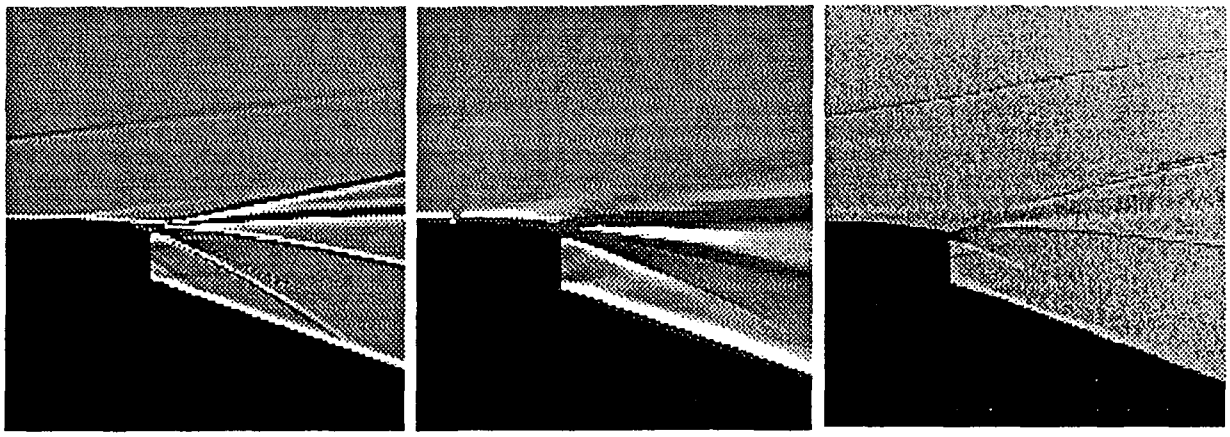

a) 2-D solution b) 3-D solution c) Experiment

Figure 4. Constructed and experimental shadowgraphs for SERN. Two-dimensional flow solution and experiment: Ruffin et al.[6]

flowfield solution in Fig. 4a is a 2-D, ideal-gas simulation at the symmetry plane; the solution in Fig. 4b is 3-D.[6] The interaction of the external flow with the nozzle plume is complicated, and all the main features observed in the experimental shadowgraph are captured in the constructed shadowgraphs. These features include the leading edge shock, separation from the nozzle, and the shocks, shear layers, and expansion fans caused by the interaction of the nozzle plume with the freestream. As with the schlieren, dark and light regions in the constructed shadowgraph correspond to dark and light regions in the experimental shadowgraph; however, in the shadowgraphs, each shock is described by the combination of a dark and light line. In the two constructed shadowgraphs, the effects of grid resolution and solution errors can be seen. The grids in the two 2-D solutions are very fine, and the constructed shadowgraph closely resembles the experimental shadowgraph. For the 3-D solution, although multiple grids were used, the gridding was much coarser than that used for the 2-D solutions. The shocks, shear layers, and expansion fans were not as well resolved in the 3-D flowfield solution and, hence, are much more diffuse in the shadowgraph.

The solutions in Figs. 3 and 4 are ideal-gas computations, and the refractive index is simply given by a constant times the density. For reacting flows, the refractive index is a function of the gas species. In Fig. 5, a constructed shadowgraph is shown for an axially-symmetric, real-gas, flowfield solution for a ballistic range shot of a hemisphere cylinder in a combustible mixture.[7,8] Also shown is an experimental shadowgraph.[9] This flow is very complex, and many of the features observed in the shadowgraph are three dimensional and difficult to identify in contour plots. In the constructed shadowgraph most if not all of the features in the experimental shadowgraph are captured, and the computations and experiment can be compared on a one-to-one basis. The ability to construct shadowgraphs facilitates the comparison of computed and experimental results, especially for very complicated flows.

In Fig. 6, a constructed and experimental infinite-fringe interferogram is shown for a ballistic range test of the Aeroassist Flight Experiment (AFE). The flowfield simulations were performed using an ideal-gas CFD solver;[10] the grid was adapted to the

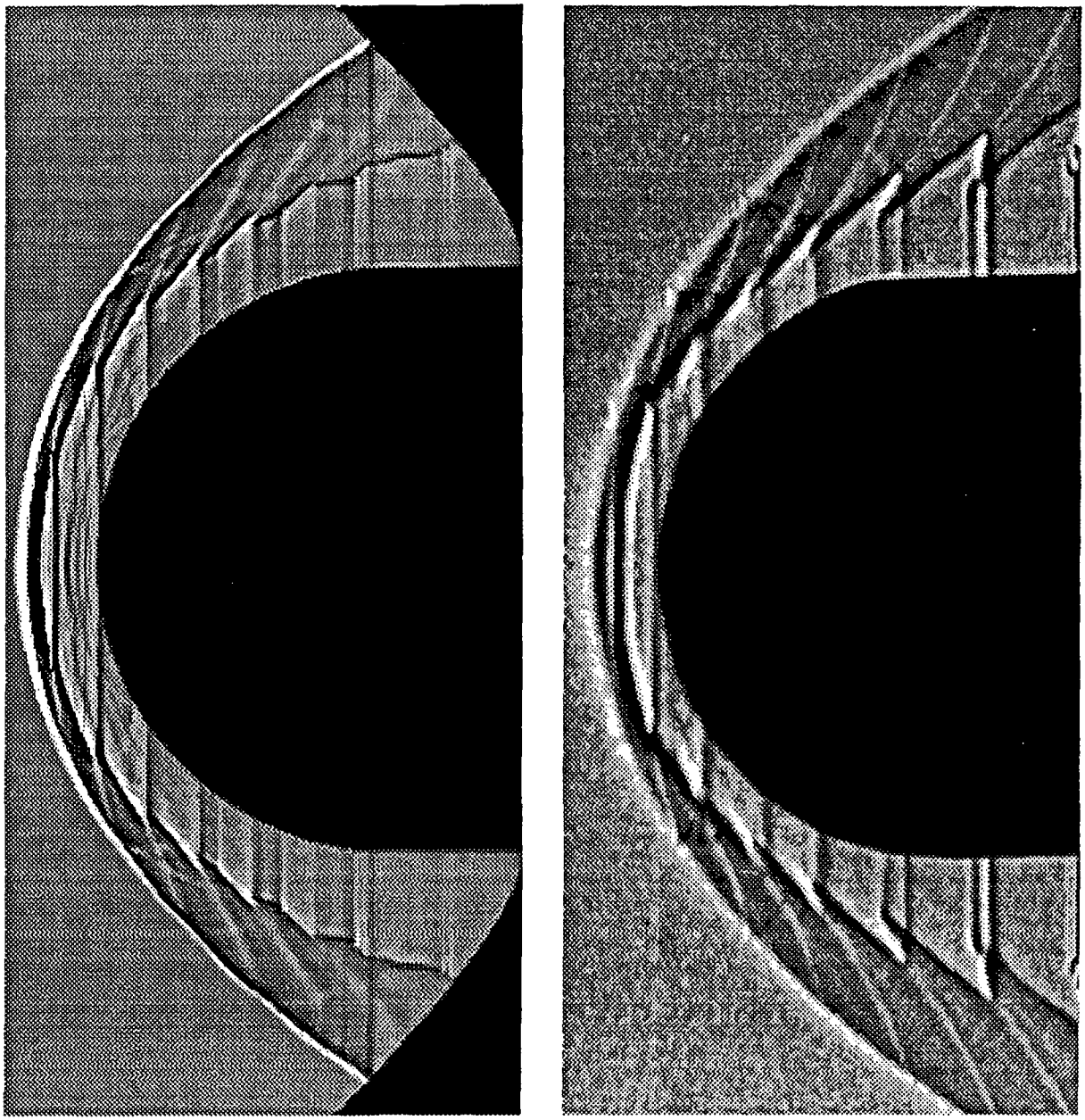

Constructed shadowgraph

Experimental shadowgraph

Figure 5. Constructed and experimental shadowgraphs for a hemisphere-cylinder in a combustible mixture. Flowfield solution: G. Wilson;[7,8] experiment: Lehr.[9]

flowfield solution using SAGE.[11] A one-to-one comparison of the two interferograms is not possible; the flowfield solution is for a model with no yaw, the experimental model did yaw. However, there are similarities. The constructed and experimental interferograms both show similar light and dark patterns, and the number of fringe shifts are comparable. The location of the fringes provides information concerning the computed and experimental integrated index of refraction.

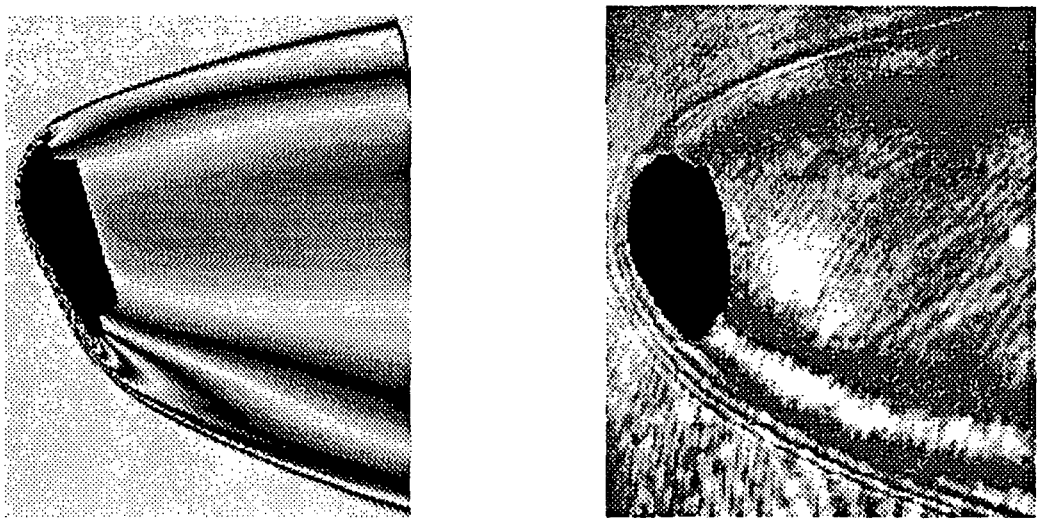

Constructed interferogram | Experimental interferogram

Figure 6. Constructed and experimental infinite-fringe interferograms for an AFE model. Three-dimensional flowfield solution: E. Venkatapathy et al.;[10] experiment performed at NASA Ames Research Center's ballistic range.

Concluding Remarks

The construction of interferograms, schlieren, and shadowgraphs from 2-D and 3-D flowfield solutions permits one-to-one comparisons of CFD and experimental results. Experimental interferograms provide quantitative information for integrals of the refractive index and density. This information can be used to verify 3-D flowfield solutions only when line of sight integrals are computed and interferograms are constructed from the flowfield solutions. The positions of shocks and shear layers are easily obtained from experimental schlieren and shadowgraphs. When contour plots are used to locate shocks and shear layers, interpretation of the contour lines is required. Furthermore, the 3-D nature of the flow is not shown. In constructed schlieren and shadowgraphs, the shocks and shear layers are defined by the same intensity variations as in the experimental images. Hence, comparison of the positions of these flow features can easily be made. In addition, 3-D effects are included in the construction.

CISS has proven its capability in constructing interferograms, schlieren, and shadowgraphs from a variety of ideal- and real-gas, 2-D, axially symmetric, and 3-D flowfield solutions. For the examples shown here, the constructed and experimental images are very similar. However, the quality of the flowfield solution does affect the quality of the constructed images. Insufficient or improperly placed grid points can cause spreading of shocks and shear layers in the constructed images. CISS not only provides an excellent tool for comparing flowfield solutions with experiment, it can be used to identify problem areas in the flowfield solutions.

Acknowledgments

Support for L. A. Yates was provided by NASA Grant NCC2-583.

References

[1]Ben-Dor, G., Whitten, B.T., and Glass, I.I., "Evaluation of Perfect and Imperfect-Gas Interferograms by Computer," *Int. J. Heat and Fluid Flow*, Vol. 1, No. 2, 1979, pp. 77-91.

[2]Shapiro, A.H., *The Dynamics and Thermodynamics of Compressible Flow*, Vol. 1, The Ronald Press Company, New York, 1953.

[3]Liepmann, H.W. and Roshko, A., *Elements of Gasdynamics*, John Wiley and Sons, New York, 1957.

[4]Tokarcik, S., Venkatapathy, E., Candler, G., and Palmer, G., "Computational Flow Predictions for Hypersonic Drag Devices," AIAA Paper 91-3303, Sept. 1991.

[5]Delery, J. and Coet, M.C., "Experiments on Shock-Wave/Boundary-Layer Interactions Produced by Two-Dimensional Ramps and Three-Dimensional Obstacles," Workshop on Hypersonic Flows for Reentry Problems, Antibes, France, Jan. 1990.

[6]Ruffin, S.M., Venkatapathy, E., Lee, S.H., Keener, E.R., and Spaid, F., "Single Expansion Ramp Nozzle Simulations" AIAA Paper 92-0387, Jan. 1992.

[7]Wilson, G.J., "Computation of Steady and Unsteady Hydrogen-Air Combustion Over Hypervelocity Blunt Bodies," Ph.D. dissertation, Stanford University, Dec. 1991.

[8]Wilson, G.J. and Sussman, M. A., "Computation of Oscillating Shock-Induced Combustion Observed in Ballistic-Range Experiments," Presented at the Fourth International Conference on Numerical Combustion, St. Petersburg, Florida, Dec. 1991.

[9]Lehr, H.F., "Experiments on Shock-Induced Combustion," Astronautica Acta, Vol. 17, pp. 589-597, 1972.

[10]Venkatapathy, E., Palmer, G., and Prabhu, D., "AFE Base Flow Computations," AIAA Paper 91-1372, June 1991.

[11]Davies, C.B. and Venkatapathy, E., "The Multi-Dimensional Self-Adaptive Grid Code, SAGE," NASA TM-103905, 1992.